Fuel 243 (2019) 262–270

Contents lists available at ScienceDirect

Fuel

journal homepage: www.elsevier.com/locate/fuel

Full Length Article

Directly catalytic reduction of NO without NH_3 by single atom iron catalyst: A DFT calculation

Weijie Yang[a], Zhengyang Gao[a,*], Xiaoshuo Liu[a], Chuanzhi Ma[a], Xunlei Ding[b,*], Weiping Yan[a]

[a] School of Energy and Power Engineering, North China Electric Power University, Baoding 071003, China
[b] School of Mathematics and Physics, North China Electric Power University, Beijing 102206, China

GRAPHICAL ABSTRACT

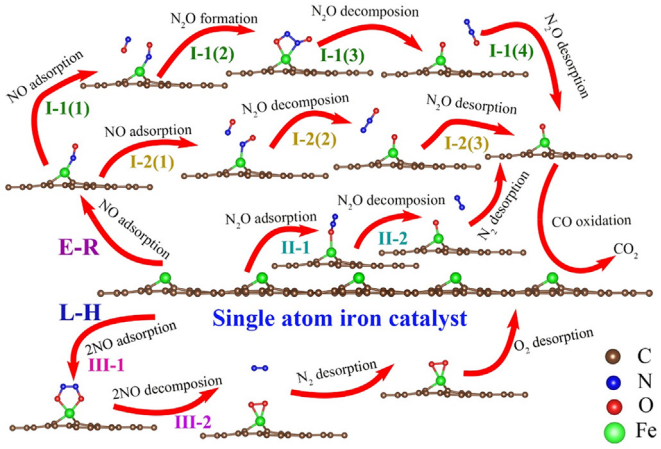

ARTICLE INFO

Keywords:
NO
Reduction
Single atom catalysis
Thermodynamic analysis
Kinetic analysis

ABSTRACT

Nitric oxide (NO) has been recognized as a major air pollutant, and the emission of NO has been strictly regulated. The technology of selective catalytic reduction of NO with NH_3 injection is mature and efficient, but it still has some obvious drawbacks such as ammonia slipping, secondary fine particulates formation, and equipment corrosion. Therefore, a directly catalytic reduction of NO without ammonia injection by mono-vacancy graphene-based single atom iron catalyst (Fe/MG) was proposed. The detailed reaction mechanism was investigated through density functional theory calculation. Based on thermodynamic and kinetic analysis, we concluded that Langmuir-Hinshelwood is the dominant reaction mechanism for NO reduction, and the activation energy is 0.81 eV which is lower than char edges. The catalytic reduction reaction of NO is exothermic and thermodynamically favorable. The temperature can accelerate the catalytic reduction of NO. Based on the thermodynamic and kinetic performances of Fe/MG in NO reduction, Fe/MG is suggested to be a novel catalyst for NO reduction without NH_3. This theoretical research results can provide a new insight for NO removal and lay some foundations for subsequent experimental research.

* Corresponding authors.
E-mail addresses: gaozhyan@163.com (Z. Gao), dingxl@ncepu.edu.cn (X. Ding).

https://doi.org/10.1016/j.fuel.2019.01.125
Received 15 December 2018; Received in revised form 16 January 2019; Accepted 23 January 2019
Available online 28 January 2019
0016-2361/

1. Introduction

Nitrogen oxide (NO_x) contains nitric oxide (NO), nitrogen dioxide (NO_2), and nitrous oxide (N_2O), which can lead to various environmental pollutions such as acid rain, photo-chemical smog and ozone depletion. NO_x released from coal-fired power plant has been considered as the main anthropogenic source, hence, the emission standard of NO_x is strictly regulated to be 50 mg/Nm^3 [1]. NO is the main component of NO_x, making it imperative to remove NO from fuel gas.

Currently, the selective catalytic reduction with ammonia injection (SCR-NH_3) has been recognized as the most mature and efficient technology for emission reduction of NO_x in coal-fired power plant. However, there are still some problems for the technology of SCR-NH3 in the operation process, such as ammonia slipping [2], secondary fine particulates formation [3], and equipment corrosion [4]. Moreover, the traditional catalysts for SCR-NH_3 (V_2O_5/TiO_2 and WO_3/TiO_2) are toxic, and will become hazardous waste after 2–3 years operation [5]. Therefore, developing a green catalyst which can directly reduce NO without ammonia injection is conducive to solve the above problems.

Single atom catalysts (SACs) are novel catalysts that can build a bridge between homogeneous catalysis and heterogeneous catalysis [6,7]. Due to its high catalytic activity, selectivity, and utilization, SACs have become the research hotspots in energy [8,9], environmental protection [10–12], and chemical engineering [13,14]. SACs have been demonstrated to have super catalytic activity in CO oxidation [15], CO_2 reduction [10,11], CH_4 activation [16] and oxygen reduction reaction [17,18]. Graphene has large specific surface area with unique physical and chemical properties, making it to be an excellent two-dimensional catalyst support. Embedding transition metal atoms into the surface of graphene-based support (TM/GS) to synthesize SACs can lower cost and improve catalytic activity [19]. Given its high catalytic activity and environment-friendly, TM/GS seems to be a potential candidate for NO reduction.

Moreover, there were some theoretical researches on the adsorption and catalytic reduction of NO under the similar system of TM/GS, which can further support and rationalize the above suppose. The adsorption of NO on the surface of metal phthalocyanines (M-PC, M = Mn, Fe, Co) was studied through density functional theory (DFT) calculation, and the adsorption energies of NO on Mn-PC, Fe-PC and Co-PC were −1.74 eV, −1.90 eV, and −1.55 eV, respectively [20]. The adsorption energies of NO and $(NO)_2$ on the surface of iron porphyrin were −2.00 eV and −2.54 eV, respectively, and the strong interaction between Fe and N may promote the reduction reaction of NO [21]. In addition, NO can be reduced into N_2O on the surface of iron porphyrin, and the energy barrier in the dimer form is 0.92 eV [21]. The energy barrier of N_2O dissociation to N_2 on the surface of Ti/GS is 2.34 eV [22], and the energy barrier of N_2O decomposition on carbon-doped boron nitride nanosheet is 2.19 eV [23]. The NO can be reduced into N_2 by CO on the surface of Ti-porphyrin, and the rate-determining step is the desorption process of CO_2 [24].

Based on the above researches, it is reasonable to assume that the catalytic reduction of NO can occur on TM/GS, and TM/GS may be a promising candidate for the catalytic reduction of NO. However, the previous researches were relatively scattered and lacked systematic investigation. Therefore, a systematic research of NO reduction on TM/GS is urgently needed to explore the feasibility of practical application at the molecular level. According to the previous studies, monovacancy graphene-based single atom iron catalyst (Fe/MG) has high catalytic activity for CO oxidation [25,26] and NO oxidation [27]. In addition, Fe/MG has high adsorptivity for many toxic gases, such as NO, CO, HCN, and SO_2 [28,29]. Therefore, it is reasonable to expect that Fe/MG has high catalytic activity on NO reduction, and Fe/MG was selected as the research catalyst.

To explore feasibility and reaction mechanism at molecule level, we investigated the directly catalytic reduction of NO without NH_3 on Fe/MG. Firstly, the adsorption characteristic of NO on Fe/MG was investigated to lay a foundation for the reaction path analysis. Secondly, the reaction paths of NO reduction on Fe/MG were systematically studied based on Langmuir-Hinshelwood (L-H) and Eley-Rideal (E-R) reaction mechanism. Additionally, thermodynamic analysis was carried out to study the effect of temperature on thermodynamic equilibrium. Moreover, the detailed kinetic analysis of two reaction mechanisms were discussed to determine the dominant mechanism. This systematic theoretical research can provide a new insight for the removal of NO and lay some foundations for subsequent experimental research.

2. Calculation method

The Perdew-Burke-Ernzerhof (PBE) functional and projector augmented wave (PAW) potentials were adopted to complete the DFT calculations [30–32], which has been proved to be an suitable method in the system of TM/GS [33,34]. In detail, the spin polarization correction was included in the calculation to consider the magnetism of Fe atom [28]. Consistent with our previous study [29], a 4 × 4 graphene with vacuum layer of 15 Å was used to simulate the surface of Fe/MG. The calculation software was Vienna ab initio simulation package (VASP 5.4.1).

To obtain accurate calculation results with less computational cost, a 7 × 7 × 1 Γ-centered k-point and 500 eV cutoff energy were adopted in the calculation of geometric optimization based on our pervious test [35,36]. With regards to geometry optimization, all atoms were allowed to fully relax with force convergence standard of 0.02 eV/Å and energy convergence standard of 10^{-5} eV. Based on the optimized geometry, a denser k-point (15 × 15 × 1) was adopted in the calculation of self-consistent field to obtain more accurate system energy, density of states (DOS), and Bader charge [37].

To locate the transition states rapidly and accurately, two methods of climbing-image nudged elastic band (CI-NEB) [38,39] and improved dimer method (IDM) [40] were applied together. Approximate structures of transition state was rapidly determined by CI-NEB method with a 0.1 eV/Å force convergence. Based on the possible transition state structures calculated by CI-NEB, the final transition state structures was accurately located by IDM with the force convergence of 0.05 eV/Å. Additionally, vibrational frequency with finite displacements of ± 0.02 Å [41,42] was calculated to validate the transition state structures and obtain the zero point energy correction.

The adsorption energy (E_{ads}) can be calculated according to Eq. (1).

$$E_{ads} = E_{tot} - E_{gas} - E_{sur} \quad (1)$$

where E_{tot}, E_{gas} and E_{sur} are the ground-state energy of adsorption systems, adsorbates, and Fe/MG, respectively.

To describe the difficulty degree of reaction process, the energy barrier (E_b) was calculated according to from Eq. (2).

$$E_b = E_{TS} - E_{IS} \quad (2)$$

where E_{TS} and E_{IS} are the system energy of transition and initial state, respectively.

Thermodynamic properties of reduction reaction was discussed through analyzing the equilibrium constant which can be calculated from the following Eq. (3) [43]:

$$\Delta G = G_{FS} - G_{IS} = -RT \cdot \ln K \quad (3)$$

where G_{FS} and G_{IS} are Gibbs free energy of final and initial state; R is the universal gas constant; T is the temperature; K is the equilibrium constant.

The Gibbs free energy of solid surface and gases was calculated from the Eqs. (4) and (5) [36]:

$$G_{solid}(T) = E_{ele} + ZPE - TS \quad (4)$$

$$G_{gas}(T) = E_{ele} + ZPE + RT - TS \quad (5)$$

where E_{ele} is the system energy in ground state obtained from self-

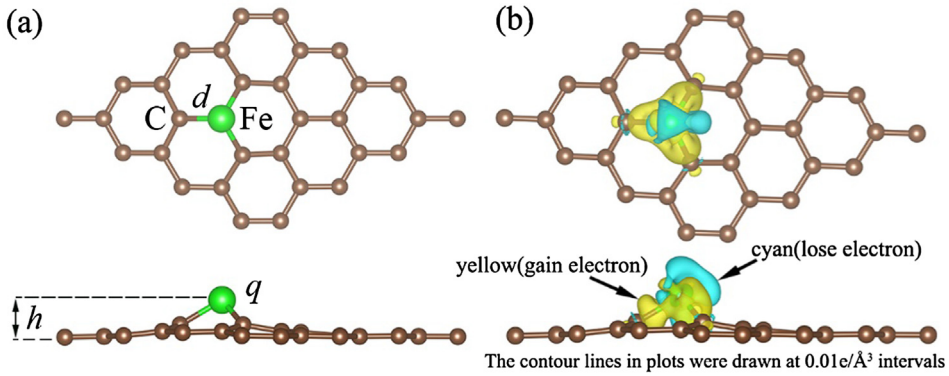

Fig. 1. The geometric structure and electron density difference of Fe/MG.

consistent field calculation; ZPE is the zero point correction energy calculated from vibrational frequency calculation; S is entropy (The entropies of adsorbed systems and gases are obtained from vibrational frequency calculation [44] and NIST database [45], respectively);

According to the transition state theory, the reaction rate constant was calculated to study the kinetic properties of reduction reaction, and the calculation formula was shown in Eq. (6) [43]:

$$k^{TST} = \frac{k_B T}{h} \times \left(\frac{RT}{P_0}\right)^{\Delta n} \times \exp\left(\frac{-\Delta G_b}{k_B T}\right) \quad (6)$$

where h is the Planck constant; k_B is the Boltzmann constant; $\Delta n = 0$ (unimolecular reaction) or 1 (bimolecular reaction); P_0 is the standard atmospheric pressure; ΔG_b is the energy barrier in Gibbs free energy.

3. Results and discussion

3.1. The research model

The optimized structure and electron density difference of Fe/MG were plotted in Fig. 1, the detailed calculation process of electron density difference can be seen in Fig. S1. The corresponding structural and electronic parameters were summarized in Table 1. From Fig. 1(b), the Fe atom was surrounded by the cyan color and the adjacent C atoms were surrounded by the yellow color, which indicates that the electron transfers from Fe atom to graphene-based supports in the doping process of Fe atom. In addition, the charge of Fe atom was 0.69 e, which is consistent with the analysis of electron density difference. According to the adsorption energy of Fe atom (Table 1), E_{ads} of Fe on monovacancy graphene (−7.14 eV) is obviously larger than that on perfect graphene (−1.04 eV [46]) and the cohesive energy of Fe bulk (−4.28 eV [47]), suggesting that Fe/MG is stable enough to avoid agglomeration and migration. Compared with the calculated results of Fe/MG and literature data, it is concluded that the research model of Fe/MG is validity and rationality.

3.2. The adsorption characteristic of NO

According to the study of Wang et al [50], Fe/MG can be a promising material for CO removal in the hydrogen fuel cells. In the research of Tang et al [28], the adsorption of NO on Fe/MG belongs to strong chemical adsorption, so Fe/MG seems to be an effective adsorbent for NO removal. To verify this assumption, the adsorption characteristic of $(NO)_n$ (n = 1–4) on Fe/MG was investigated. The optimized adsorption structures of $(NO)_n$ (n = 1–4) on Fe/MG were plotted in Fig. 2(a)–(d), and some important adsorption configurations for reaction path analysis were also plotted in Fig. 2(e)–(h). Additionally, some key parameters in adsorption process, such as adsorption energies, bond lengths and charge transfer, were summarized in Table 2.

Table 1
The bond length between C and Fe (d), the uplift height of Fe (h), the charge of Fe (q) and the adsorption energy of Fe (E_{ads}) for Fe/MG.

Systems	d (Å)	h (Å)	q (e)	E_{ads} (eV)
Calculation data	1.76	1.35	0.69	−7.14
Literature data	1.76 [26]	1.36 [48]	0.69 [36]	−7.15 [49], −7.28 [26]

Combining the Table 2 and Fig. 2(a–d), the E_{ads} increased as the number of NO increased, while the $E_{ads/per}$ decreased as the number of NO increased. Meanwhile, the average bond length between N and Fe ($d_{N\text{-}Fe}$) increased as the number of NO increased, indicating that the adsorption strength decreases as the number of NO increases. The $d_{N\text{-}Fe}$ obviously increased from 1.74 Å to 1.94 Å when the third NO molecule was adsorbed on Fe/MG, and the $d_{N\text{-}Fe}$ obviously increased from 1.94 Å to 2.27 Å when the fourth NO molecule was adsorbed on Fe/MG. From the adsorption configurations of NO on Fe/MG, the maximum bond lengths between N and Fe in Fig. 2(c) and (d) were 2.13 Å and 3.15 Å, further confirming that the adsorption strength of NO on Fe/MG obviously decreases when the number of NO molecule increases to three. Different from the study of Wang et al on CO adsorption [50], Fe/MG can firmly adsorb three CO molecules at the same time, but only two NO molecules can be firmly adsorbed on Fe/MG. Therefore, Fe/MG may not be suitable as an adsorbent for NO removing, and a detailed analysis focused on the catalytic reduction mechanism was carried out in the next content.

From Table 2, it is noteworthy that there is a clear linear relationship between the amounts of charge transfer and the adsorption energies of NO on Fe/MG, except for Fig. 2(g). There was a −3.65 eV adsorption energy with 0.49 e charge transfer for the adsorption configuration of Fig. 2(b), but there was a −3.35 eV adsorption energy with 0.91 e for the adsorption configuration of Fig. 2(g). In order to investigate the difference between Fig. 2(b) and (g) in adsorption energy and charge transfer, the bonding characteristics of adsorption configurations in Fig. 2(b) and (g) were discussed through the projected density of states (PDOS) analysis. The PDOS of Fig. 2(b) and (g) were plotted in Figs. 3 and 4, respectively. In detail, density of states for total, d orbital of Fe atom and p orbital of two N or O atoms in NO molecules were plotted to study the interaction of Fe/MG and NO. According to the frontier molecular orbital theory, regions near Fermi energy level are critical for bonding, so some regions were circled by broken lines to investigate the hybridization between NO and Fe/MG. In the regions circled by broken lines of Fig. 3, the peaks of Fe(d) and N(p) occur at the same energy level, suggesting that there was strong hybridization between Fe(d) and N(p). However, there was no obvious strong hybridization between Fe(d) and O(p) in the regions circled by broken lines of Fig. 4. From the above analysis, it is deduced that the binding mechanism adsorption configuration of Fig. 2(g) is dominated by hybridization effect, whereas the binding mechanism adsorption

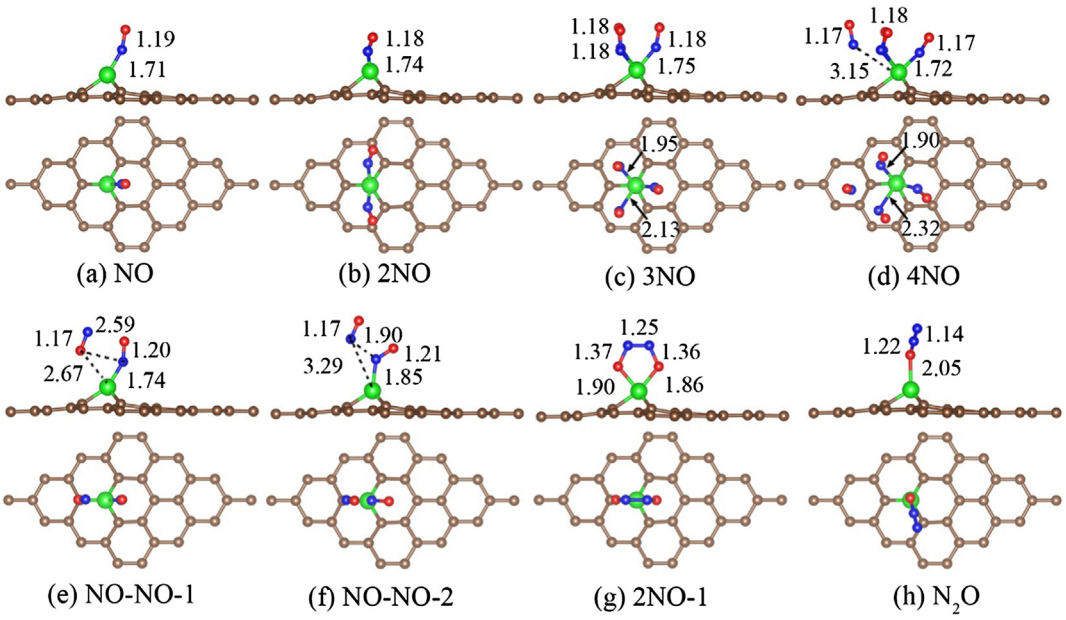

Fig. 2. The adsorption structures of NO on Fe/MG (The unit of length is Å).

Table 2
The adsorption energies of NO (E_{ads}, eV), the adsorption energy per NO ($E_{ads/per}$, eV), the average bond lengths between N and Fe ($d_{N\text{-}Fe}$, Å) and the charge variations of corresponding gases before and after adsorption (Δq, e). (The symbol of "+" and"−" means gain and lose electron).

Structures	E_{ads} (eV)	$E_{ads/per}$ (eV)	$d_{N\text{-}Fe}$ (Å)	$\Delta q_{\text{-gas}}$ (e)
(a) NO	−2.24 (−2.40 [28])	−2.24	1.71	+0.34 (+0.43 [28])
(b) 2NO	−3.65	−1.82	1.74	+0.49
(c) 3NO	−3.98	−1.33	1.94	+0.55
(d) 4NO	−4.61	−1.15	2.27	+0.63
(e) NO-NO-1	−2.64	−1.32	2.21	+0.41
(f) NO-NO-2	−2.56	−1.28	2.57	+0.38
(g) 2NO-1	−3.35	−1.67	–	+0.91
(h) N_2O	−0.38	−0.38	–	+0.07

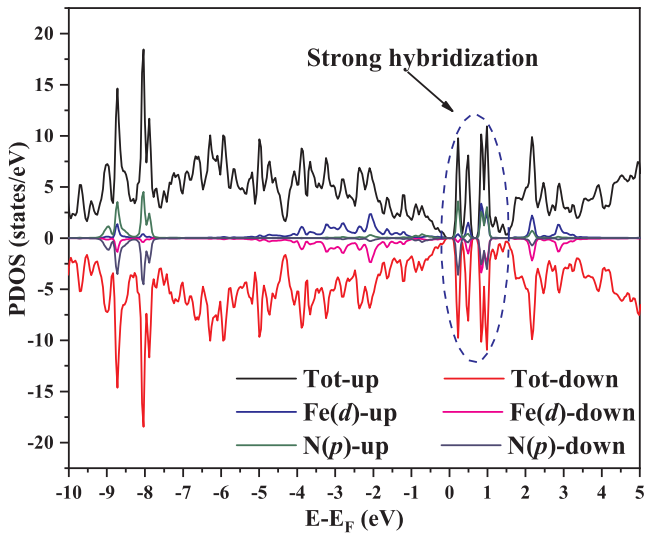

Fig. 3. The PDOS for the structure of Fig. 2(b).

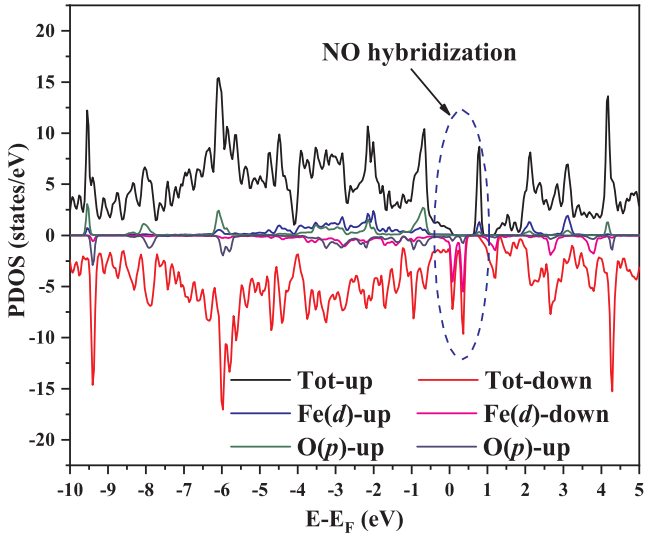

Fig. 4. The PDOS for the structure of Fig. 2(g).

configuration of Fig. 2(b) is mainly governed by charge transfer. Therefore, the difference between Fig. 2(b) and (g) in adsorption energy and charge transfer can be well understood from the view of binding mechanism.

To study the catalytic reduction of NO on Fe/MG, the possible adsorption configurations of NO and N_2O on Fe/MG were calculated according to the reaction mechanism of Eley-Rideal (E-R) and Langmuir-Hinshelwood (L-H), as show in Fig. 2(e)–(h). There were two possible adsorption structures of NO on Fe/MG in Fig. 2(e) and (f). Given that there is no obvious difference between two possible adsorption configurations in adsorption energy, therefore, Fig. 2(e) and (f) were both selected as the initial reactants for E-R mechanism analysis. At the same time, the adsorption configurations of Fig. 2(b) and (g) were both selected as the initial reactants for L-H mechanism analysis.

3.3. Reaction path analysis

To consider the E-R and L-H reaction mechanism, we designed various reaction paths based on the adsorption configurations of two

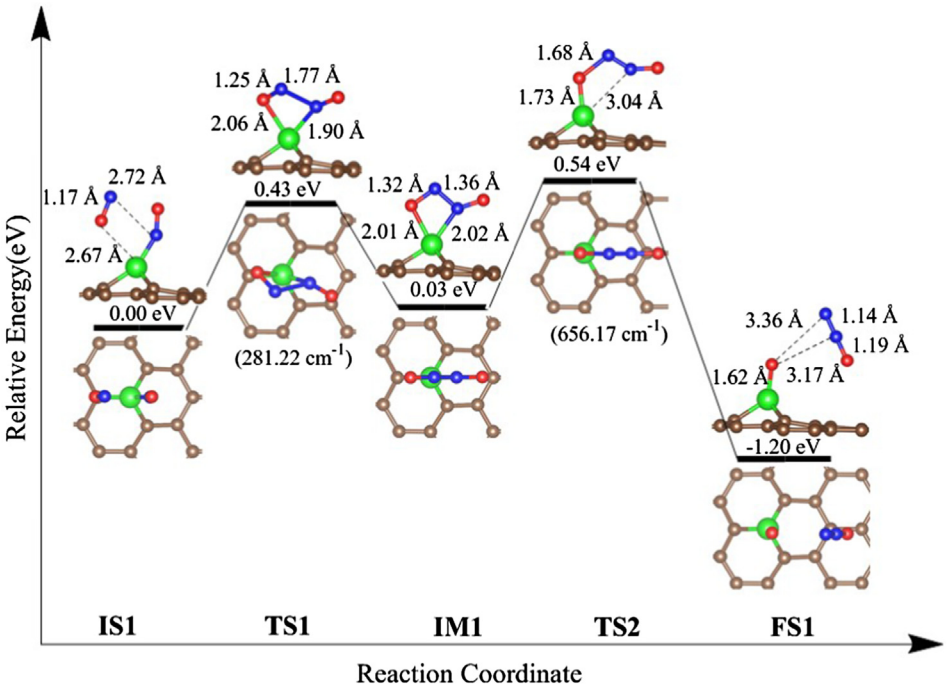

Fig. 5. The reduction reaction path diagram of NO into N_2O (E-R-I-1).

NO molecules on Fe/MG (Fig. 2(b), (e)–(g)). However, no possible reaction path was found when the adsorption configuration of Fig. 2(b) was selected as initial reactant. Therefore, the reaction path in the L-H mechanism analysis which only started from Fig. 2(g), was elaborated in this work. Based on the E-R and L-H reaction mechanism, the reaction path analysis was performed respectively. Furthermore, in E-R reaction mechanism, the catalytic reduction of NO can be divided into two different reaction stages according to the reaction process. The first stage is the catalytic reduction of NO into N_2O (E-R-I), and the second stage is the catalytic reduction of N_2O into N_2 (E-R-II).

3.3.1. E-R reaction mechanism

3.3.1.1. The reduction of NO into N_2O. According to the different adsorption configurations of the second NO molecule (Fig. 2(e) and (f)), there were two different reaction paths for the catalytic reduction of NO (E-R-I-1 and E-R-I-2), and the detailed reaction path diagrams were plotted in Figs. 5 and 6, respectively. In detail, the key bond length, the change of system energy (ZPE was included), and the imaginary frequency of transition state were labeled in Figs. 5 and 6.

In Fig. 5, the catalytic reduction of NO on Fe/MG started from the adsorption configuration of Fig. 2(e), and two NO molecules were reduced into N_2O on Fe/MG through two transition states. Firstly, the gaseous NO molecule attacked NO which was adsorbed on Fe/MG, generating a N_2O molecule with an energy barrier of 0.43 eV. Then, with the increase of Fe-N bond length (2.02 Å (IM1) → 3.04 Å (TS2) → 3.17 Å (FS1)), the formed N_2O molecule desorbed from Fe/MG with an energy barrier of 0.51 eV.

In Fig. 6, the catalytic reduction of NO on Fe/MG started from the adsorption configuration of Fig. 2(f), and two NO molecules were reduced into N_2O on the surface of Fe/MG through only one transition state. The NO molecule attacked the N atom of NO adsorbed on Fe/MG, and the formation and desorption of N_2O were completed at the same time with the decrease of N-N bond length (1.90 Å (IS2) → 1.27 Å (TS3) → 1.14 Å (FS2)) and the increase of N-O bond length (1.21 Å (IS2) → 1.41 Å (TS3) → 3.22 Å (FS2)). Compared with the reaction path E-R-I-1 (Fig. 5), the energy barrier of catalytic reduction is 0.21 eV, which is smaller than that in E-R-I-1 (0.43 eV and 0.51 eV). Although the adsorption energy in Fig. 2(e) is relatively larger than that in Fig. 2(f), the catalytic reduction of NO in E-R-I-2 is more likely to occur than in E-R-I-1 at the view of reaction process and energy barrier.

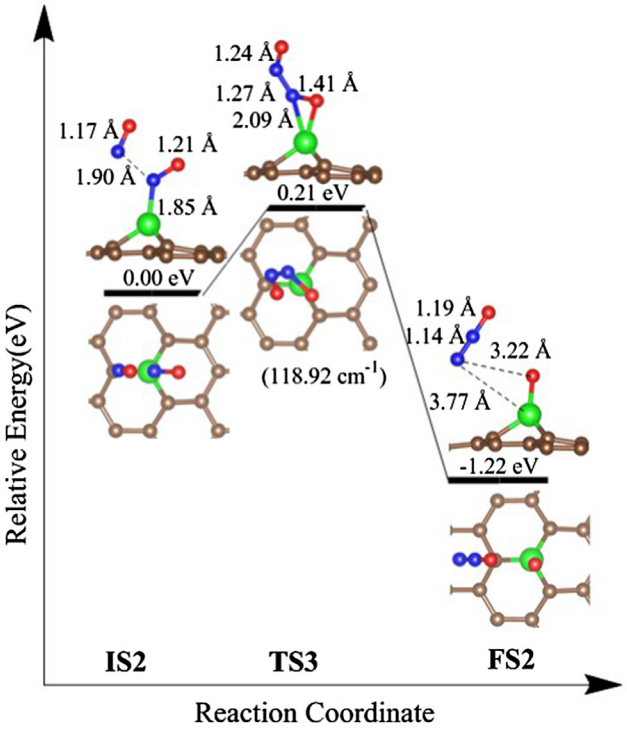

Fig. 6. The reduction reaction path diagram of NO into N_2O (E-R-I-2).

3.3.1.2. The reduction of N_2O into N_2. Two NO molecules can be reduced into N_2O relatively easily on Fe/MG according to the above analysis, and the reduction of N_2O into N_2 will be discussed in this content. The formed N_2O molecule can be reduced into N_2 on Fe/MG, the detailed reaction path was plotted in Fig. 7. From Fig. 7, with the increase of N-O bond length (1.22 Å (IS3) → 1.39 Å (TS4) → 3.07 Å

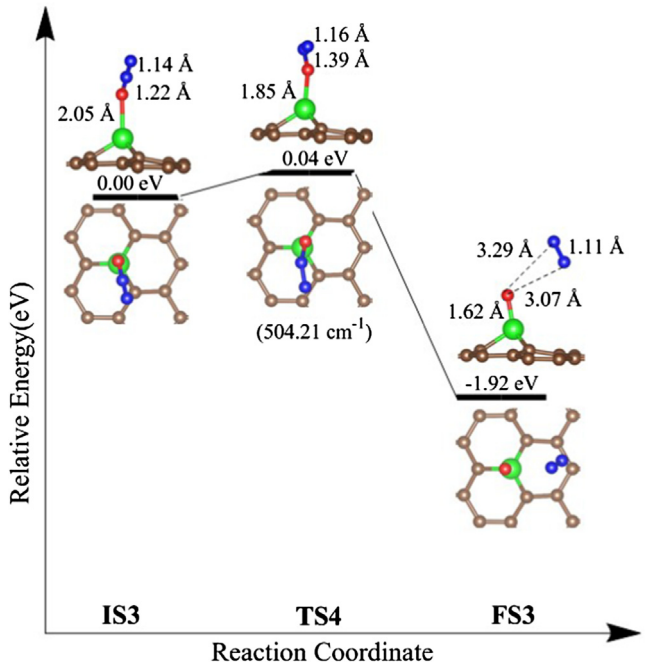

Fig. 7. The reduction reaction path diagram of N_2O into N_2 (E-R-II).

(FS3)), the N_2O molecule was decomposed into N_2 under the catalytic effect of Fe/MG. The decomposition of N_2O into N_2 can easily take place with a 0.04 eV energy barrier, and the decomposition of N_2O is an exothermic process (1.92 eV). The decomposition of N_2O is barrierless and thermodynamically favorable, so the decomposition of N_2O can take place at the room temperature. Compared with the reduction of N_2O into N_2 on the surface of Co/SV [51], the energy barrier of on Fe/MG (0.04 eV) is lower than that on Co/SV (0.1 eV), indicating that Fe/MG has higher catalytic activity than Co/SV.

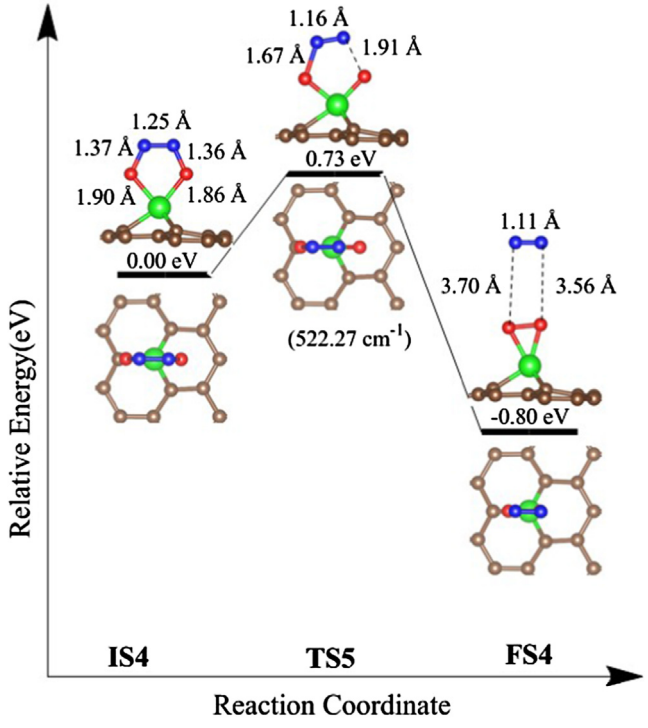

Fig. 8. The reaction path diagram of NO reduction (L-H).

3.3.2. L-H mechanism

In L-H mechanism, the catalytic reduction of NO started from Fig. 2(g), and the detailed reaction path was plotted in Fig. 8. From Fig. 8, two adsorbed NO molecules was activated under the activation effect of Fe/MG, the N-O bond lengths of two adsorbed NO molecules (1.36 Å and 1.37 Å) are all larger than the bond length of gaseous NO molecule (1.15 Å) [52]. With the increase of N-O bond length (1.37 Å (IS4) → 1.67 Å (TS5) → 3.70 Å (FS4) and 1.36 Å (IS4) → 1.91 Å (TS5) → 3.56 Å (FS4)), the N_2 molecule desorbed from Fe/MG through a medium energy barrier (0.73 eV). Similar to E-R mechanism, the reduction reaction was also exothermic progress (0.80 eV) in L-H mechanism.

For recover of catalyst, the desorption process of residual oxygen atom and O_2 adsorbed on the surface of Fe/MG should be investigated. Many studies have shown that the residual oxygen atom and O_2 adsorbed on the surface of Fe/MG can react with CO to produce CO_2 with a low energy barrier [25,26]. There are about 500 ppm CO in the flue gases, and the residual oxygen atom should be easily consumed by CO. Given that the main purpose of this study is to reveal the mechanism of NO catalytic reduction, so the detailed reaction paths between residual oxygen (O atom and O_2) and CO will not be discussed in this work.

Comparing E-R mechanism and L-H mechanism, the catalytic reduction of NO in E-R and L-H mechanism were both exothermic process and thermodynamically favorable. The catalytic reduction of NO in L-H mechanism occurred through only one transition state, but there were two stages for catalytic reduction of NO in E-R mechanism. However, the energy barrier in E-R mechanism is relatively lower than that in L-H mechanism. To further investigate the effect of temperature on the catalytic reduction of NO and confirm its dominant mechanism in E-R and L-H, the thermodynamic analysis and kinetic analysis were performed to discuss this in detail.

3.4. Thermodynamic analysis

To investigate the effect of temperature on the thermodynamic properties of catalytic reduction of NO and compare the difference of E-R and L-H mechanism in thermodynamic properties, the reaction Gibbs free energy (ΔG) and equilibrium constant (K) were calculated. Given the temperature of fuel gas, the research temperature range was selected from 298.15 K to 1000 K. The value of ΔG were summarized in Table S1 (ESI). According to the Eq. (3), the natural logarithm of K for different reaction paths were calculated, as shown in Fig. 9.

From Table S1, except for IS1 → IM1, the reaction energies of different reaction steps under research temperature range were all negative, which indicates that the most reaction steps of NO reduction can

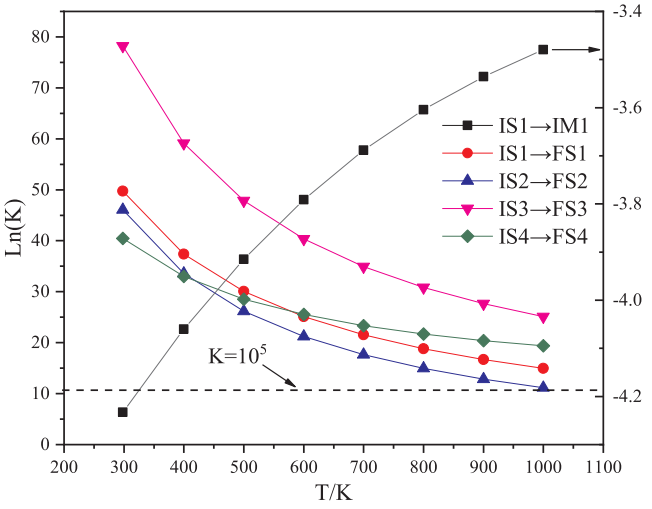

Fig. 9. The Ln(K) under different temperatures.

occur spontaneously under the research temperature range. In Fig. 9, the Ln(K) data of IS1 → IM1 was plotted in right coordinate axis, and Ln (K) data of the others were plotted in left coordinate axis. From Fig. 9, the Ln(K) data of IS1 → FS1 increased with the increase of temperature, whereas the Ln(K) data of the others decreased with the increase of temperature. For the reaction steps of IM1 → FS1, IS2 → FS2, IS3 → FS3 and IS4 → FS4, the temperature has obvious inhibiting effect on reaction equilibrium, and higher temperature will promote the reaction equilibrium to the adverse direction. Although the value of Ln(K) decreased with the increase of temperature, the Ln(K) data of IM1 → FS1, IS2 → FS2, IS3 → FS3 and IS4 → FS4 under different temperatures were all larger than 10^5 [43], illustrating that the reaction rate of forward direction will be far greater than that of reverse direction and those reaction steps can take place completely and irreversibly. Therefore, the reaction steps of IM1 → FS1, IS2 → FS2, IS3 → FS3 and IS4 → FS4 were treated as unidirectional and forward reaction in the following kinetic analysis.

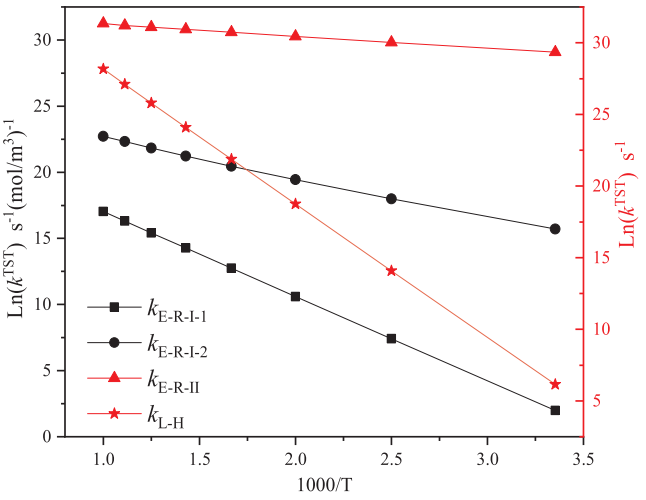

Fig. 11. The Ln(k^{TST}) for different reaction steps.

3.5. Kinetic analysis

To consider the effect of temperature on the kinetic characteristics of catalytic reduction of NO and compare the difference of E-R and L-H mechanism in kinetic properties, the natural logarithm of reaction rate constants (Ln(k^{TST})) were calculated according to the Eq. (6). The Ln (k^{TST}) of elementary reactions in bimolecular and unimolecular reaction were plotted in Fig. 10. The reaction rate constants of forward process were marked by positive number (such as k_1) and the reaction rate constants of reverse process were marked by negative number (such as k_{-1}). From Fig. 10, the reaction rate constants all increased with the increase of temperature. The Ln(k^{TST}) of forward processes were all greater than zero under all of the research temperatures, whereas Ln (k^{TST}) of forward processes were mostly less than zero under most of the research temperatures. The reaction rate constants of forward processes (except for the reaction of IS1 to IM1) were all far greater than that of reverse processes, which is in accordance with thermodynamic analysis, suggesting that the catalytic reduction of NO will be mainly governed by the forward process under the research temperature range.

In order to compare the reaction rate constant of E-R and L-H conveniently, the overall reaction rate constants in E-R and L-H mechanism were further discussed in the next analysis. According to the above reaction path analysis, there was no obvious difference between two transition states in energy barrier for E-R-I-1 reaction path. Therefore, the steady state approximation theory [53], which has been proved to be reasonable for kinetics modeling, was adopt for calculating the overall reaction rate constant in E-R mechanism. In steady state approximation theory, the concentration of intermediates involved in the reaction is considered not to vary with time. The overall reaction rate constant of E-R-I-1 ($k_{E-R-I-1}$) can be calculated by Eq. (7), and the detailed derivation was provided in the supporting material (ESI).

$$k_{E-R-I-1} = \frac{k_1 k_2}{k_{-1} + k_2} \tag{7}$$

In addition, the overall reaction rate constants of E-R-I-2 ($k_{E-R-I-2}$), E-R-II (k_{E-R-II}) and L-H (k_{L-H}) are equal to k_3, k_4 and k_5, respectively. Therefore, the reaction rate constant of different reaction steps can be easily obtained based on the above reaction rate constant calculation, as shown in Fig. 11.

In Fig. 11, the bimolecular reactions and the unimolecular reactions were plotted in the black and red color, respectively. Based on above reaction rate constants, the pre-exponential factor (A) and activation energy (E_a) were calculated. The detailed calculation steps and data were provided in Fig. S2 and Table 3, respectively. From Table 3, the activation energy of the reduction of N_2O into N_2 is only 0.07 eV, which is obviously lower than that of N_2O reduction on the surface of zigzag char edges (0.34 eV) and armchair char edges (1.64 eV) [43]. Comparing the activation energy of Fe/MG and char edges, the lower activation energy of Fe/MG indicates that the Fe/MG has higher catalytic activity than the char.

Given that there were two reaction paths in the first stage of E-R mechanism, it is inconvenient to directly compare the speed of E-R and

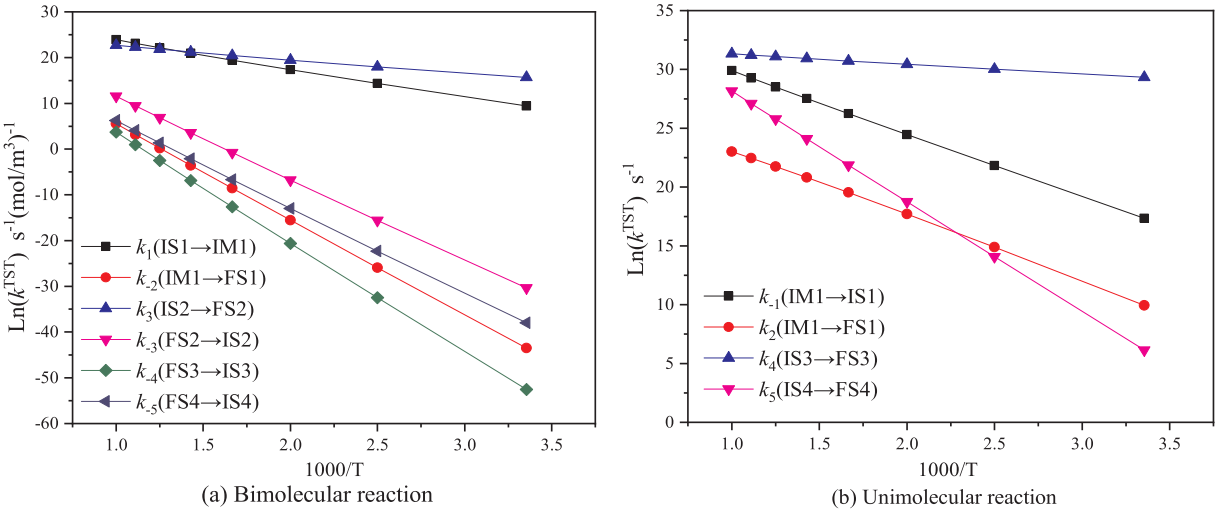

Fig. 10. The natural logarithm of reaction rate constants for different elementary reactions.

Table 3
The kinetic parameters of different reaction steps.

Kinetic parameters	E-R-I-1	E-R-I-2	E-R-II	L-H
E_a/eV	0.55	0.25	0.07	0.81
A	$1.46 \times 10^{10}\,s^{-1}\,(mol/m^3)^{-1}$	$1.20 \times 10^{11}\,s^{-1}\,(mol/m^3)^{-1}$	$9.17 \times 10^{13}\,s^{-1}$	$1.87 \times 10^{16}\,s^{-1}$

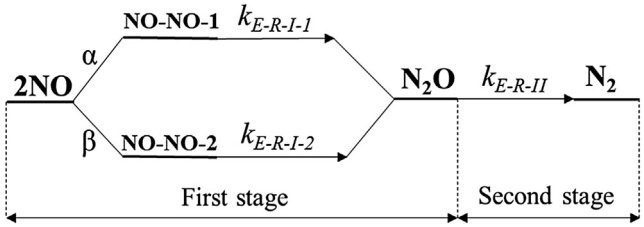

Fig. 12. The schematic diagram of catalytic reaction in E-R mechanism.

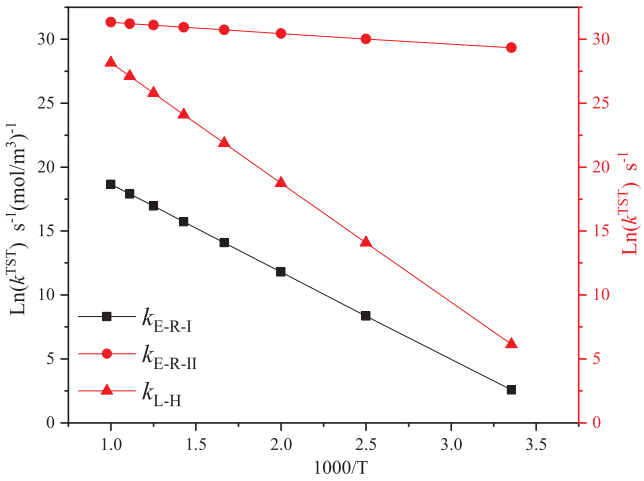

Fig. 13. The overall reaction rate constant for different reaction mechanisms.

L-H mechanisms. Therefore, the overall reaction rate constant of first stage in E-R mechanism (k_{E-R-I}) which includes the contribution of two pathways to the reaction rate, should be calculated. To obtain the value of k_{E-R-I}, the schematic diagram of catalytic reaction in E-R mechanism was plotted, as shown in Fig. 12.

In Fig. 12, due to different adsorption configurations (as shown in Fig. 2), there were two reaction paths in the first stage of reaction. The proportions of two adsorption configurations were α and β, and the sum of α and β is equal to 1 (α + β = 1). According to the Boltzmann distribution [50], we can get the proportional relationship between α and β using the adsorption energy from Table 2, and the detailed calculation was shown in Eq. (8).

$$\frac{\alpha}{\beta} = \exp\left(-\frac{E_{ads(NO-NO-1)} - E_{ads(NO-NO-2)}}{k_B T}\right) \quad (8)$$

Therefore, the value of α and β can be calculated and the detailed data was summarized in Table S2. The overall reaction rate constant of first stage in E-R mechanism (k_{E-R-I}) was calculated from Eq. (9), and the value of k_{E-R-I} was plotted in Fig. 13.

$$k_{E-R-I} = \alpha k_{E-R-I-1} + \beta k_{E-R-I-2} \quad (9)$$

From Fig. 13, the overall reaction rate constant of second stage (k_{E-R-II}) in E-R mechanism is obviously larger than that of first stage (k_{E-R-I}), indicating that the reaction speed is determined by the first stage in E-R mechanism. Comparing the value of k_{E-R-I} and k_{L-H}, k_{L-H} is larger than k_{E-R-I}, especially in high temperature. Therefore, the dominant mechanism should be L-H in the view of kinetic properties. The activation energy of NO reduction in L-H mechanism is 0.81 eV. In the catalytic reduction of NO on char edges [54], the dominant reaction mechanism of NO reduction on the surface of char edges is E-R mechanism, and the activation energy of NO reduction on the surface of char edges is 1.08 eV. Compared with the reduction of NO on char edges, the catalytic reduction of NO on the surface of Fe/MG has lower activation energy, further confirming that Fe/MG can be a promising catalyst for NO reduction.

4. Conclusion

In this theoretical research work, the mechanism of directly catalytic reduction of NO on Fe/MG was systematically studied based on the reaction path, thermodynamic and kinetic analysis. The catalytic reduction of NO in E-R mechanism can be divided into two different stages, and the rate-determining step is the first stage (the reduction of two NO molecules into N_2O). The reaction of second stage (the reduction of N_2O into N_2) can be considered as barrierless with an activation energy of 0.07 eV. The catalytic reduction reactions of NO in L-H and E-R mechanisms are both exothermic and thermodynamically favorable. The L-H mechanism acts as the dominant role in the view of reaction kinetics, and its activation energy of NO reduction on the surface of Fe/MG is 0.81 eV. In addition, the temperature acts as a promoting effect on the catalytic reduction of NO. Based on the thermodynamic and kinetic performances of Fe/MG in NO reduction reaction, Fe/MG is suggested to be a novel catalyst for directly catalytic reduction of NO without NH_3.

Acknowledgements

This work was supported by the National Natural Science Foundation of China (No. 91545122), Beijing Natural Science Foundation (2182066), Natural Science Foundation of Hebei Province of China (B2018502067) and the Fundamental Research Funds for the Central Universities (JB2015RCY03 and 2017XS121). Computational resources from the Lvliang Supercomputer Center were acknowledged.

Appendix A. Supplementary data

Supplementary data to this article can be found online at https://doi.org/10.1016/j.fuel.2019.01.125.

References

[1] Li M, Klimont Z, Zhang Q, Martin RV, Zheng B, Heyes C, et al. Comparison and evaluation of anthropogenic emissions of of SO_2 and NO_x over China. Atmos Chem Phys 2018;18:3433–56.
[2] Chen W, Qu Z, Huang W, Hu X, Yan N. Novel effect of SO_2 on selective catalytic oxidation of slip ammonia from coal-fired flue gas over IrO_2 modified Ce–Zr solid solution and the mechanism investigation. Fuel 2016;166:179–87.
[3] Chen W, Ma Y, Yan N, Qu Z, Yang S, Xie J, et al. The co-benefit of elemental mercury oxidation and slip ammonia abatement with SCR-Plus catalysts. Fuel 2014;133:263–9.
[4] Maqbool MS, Pullur AK, Ha HP. Novel sulfation effect on low-temperature activity enhancement of CeO2-added Sb-V2O5/TiO2 catalyst for NH3-SCR. Appl Catal, B 2014;152–153:28–37.
[5] Yu Y, He C, Chen J, Meng X. Deactivation mechanism of de-NO_x catalyst (V_2O_5-WO_3/TiO_2) used in coal fired power plant. J Fuel Chem Technol 2012;40:1359–65.
[6] Wang A, Li J, Zhang T. Heterogeneous single-atom catalysis. Nat Rev Chem 2018.
[7] Liang S, Hao C, Shi Y. The power of single-atom catalysis. ChemCatChem 2015;7:2559–67.
[8] Xue Y, Huang B, Yi Y, Guo Y, Zuo Z, Li Y, et al. Anchoring zero valence single atoms of nickel and iron on graphdiyne for hydrogen evolution. Nat Commun 2018;9:1460.

[9] Shi Y, Zhao C, Wei H, Guo J, Liang S, Wang A, et al. Single-atom catalysis in mesoporous photovoltaics: the principle of utility maximization. Adv Mater 2014;26:8147–53.
[10] Zhang C, Yang S, Wu J, Liu M, Yazdi S, Ren M, et al. Electrochemical CO_2 reduction with atomic iron-dispersed on nitrogen-doped graphene. Adv Energy Mater 2018. 1703487.
[11] Yang HB, Hung S-F, Liu S, Yuan K, Miao S, Zhang L, et al. Atomically dispersed Ni(i) as the active site for electrochemical CO_2 reduction. Nat Energy 2018;3:140–7.
[12] Gao C, Chen S, Wang Y, Wang J, Zheng X, Zhu J, et al. Heterogeneous single-atom catalyst for visible-light-driven high-turnover CO_2 reduction: the role of electron transfer. Adv Mater 2018;30:e1704624.
[13] Lin J, Wang A, Qiao B, Liu X, Yang X, Wang X, et al. Remarkable performance of Ir_1/FeO_x single-atom catalyst in water gas shift reaction. J Am Chem Soc 2013;135:15314–7.
[14] Liu W, Zhang L, Liu X, Liu X, Yang X, Miao S, et al. Discriminating catalytically active FeN_x species of atomically dispersed Fe-N-C catalyst for selective oxidation of the C-H bond. J Am Chem Soc 2017.
[15] Qiao B, Wang A, Yang X, Allard LF, Jiang Z, Cui Y, et al. Single-atom catalysis of CO oxidation using Pt_1/FeO_x. Nat Chem 2011;3:634–41.
[16] Yan-Xia Z, Zi-Yu L, Zhen Y, Xiao-Na L, Sheng-Gui H. Thermal methane conversion to formaldehyde promoted by single platinum atoms in $PtAl_2O_4$ cluster anions. Angew Chem 2014;53:9482–6.
[17] Chen Y, Ji S, Wang Y, Dong J, Chen W, Li Z, et al. Isolated single iron atoms anchored on N-doped porous carbon as an efficient electrocatalyst for the oxygen reduction reaction. Angew Chem 2017;129:7041–5.
[18] Chen X, Yu L, Wang S, Deng D, Bao X. Highly active and stable single iron site confined in graphene nanosheets for oxygen reduction reaction. NANO Energy 2017;32:353–8.
[19] Bayatsarmadi B, Zheng Y, Vasileff A, Qiao S-Z. Recent advances in atomic metal doping of carbon-based Nanomaterials for energy conversion. Small 2017;13:1700191.
[20] Nguyen TQ, Escaño MCS, Kasai H. Nitric oxide adsorption effects on metal phthalocyanines. J Phys Chem B 2010;114:10017–21.
[21] Ashori E, Nazari F, Illas F. Influence of NO and $(NO)_2$ adsorption on the properties of Fe-N4 porphyrin-like graphene sheets. Phys Chem Chem Phys 2017;19:3201–13.
[22] Esrafili MD, Saeidi N, Dinparast L. A DFT study on catalytic epoxidation of ethylene over Ti-doped graphene nanoflake in the presence of NO molecules. Chem Phys Lett 2017;687:290–6.
[23] Esrafili MD, Saeidi N. Carbon-doped boron nitride nanosheet as a promising catalyst for N_2O reduction by CO or SO_2 molecule: a comparative DFT study. Appl Surf Sci 2018;444:584–9.
[24] Harrath K, Boughdiri S. High catalytic activity of Ti-porphyrin for NO reduction by CO: a first-principles study. Res Chem Intermed 2017;44:957–69.
[25] Li Y, Zhou Z, Yu G, Chen W, Chen Z. CO catalytic oxidation on iron-embedded graphene: computational quest for low-cost nanocatalysts. J Phys Chem C 2010;114:6250–4.
[26] Tang Y, Zhou J, Shen Z, Chen W, Li C, Dai X. High catalytic activity for CO oxidation on single Fe atom stabilized in graphene vacancies. RSC Adv 2016;6:93985–96.
[27] Tang Y, Liu Z, Shen Z, Chen W, Ma D, Dai X. Adsorption sensitivity of metal atom decorated bilayer graphene toward toxic gas molecules (CO, NO, SO_2 and HCN). Sens Actuators, B 2017;238:182–95.
[28] Yang W, Gao Z, Liu X, Li X, Ding X, Yan W. Catal Sci Technol 2018;8:4159–68.
[29] Shi LB, Wang YP, Dong HK. First-principle study of structural, electronic, vibrational and magnetic properties of HCN adsorbed graphene doped with Cr, Mn and Fe. Appl Surf Sci 2015;329:330–6.
[30] Perdew JP, Burke K, Ernzerhof M. Generalized gradient approximation made simple. Phys Rev Lett 1996;77:3865.
[31] Kresse G, Furthmüller J. Efficiency of ab-initio total energy calculations for metals and semiconductors using a plane-wave basis set. Comput Mater Sci 1996;6:15–50.
[32] Kresse G, Furthmüller J. Efficient iterative schemes for ab initio total-energy calculations using a plane-wave basis set. Phys Rev B 1996;54:11169.
[33] Liu SG, Huang SP. Theoretical insights into the activation of O_2 by Pt single atom and Pt_4 nanocluster on functionalized graphene support: critical role of Pt positive polarized charges. Carbon 2017;115:11–7.
[34] Liu L-L, Chen C-P, Zhao L-S, Wang Y, Wang X-C. Metal-embedded nitrogen-doped graphene for H_2O molecule dissociation. Carbon 2017;115:773–80.
[35] Gao Z, Yang W, Ding X, Lv G, Yan W. Support effects on adsorption and catalytic activation of O2 in single atom iron catalysts with graphene-based substrates. Phys Chem Chem Phys 2018;20:7333–41.
[36] Gao Z, Yang W, Ding X, Lv G, Yan W. Support effects in single atom iron catalysts on adsorption characteristics of toxic gases (NO_2, NH_3, SO_3 and H_2S). Appl Surf Sci 2018;436:585–95.
[37] Tang W, Sanville E, Henkelman G. A grid-based Bader analysis algorithm without lattice bias. J Phys: Condens Matter 2009;21:084204.
[38] Henkelman G, Uberuaga BP, Jónsson H. A climbing image nudged elastic band method for finding saddle points and minimum energy paths. J Chem Phys 2000;113:9901–4.
[39] Henkelman G, Jónsson H. Improved tangent estimate in the nudged elastic band method for finding minimum energy paths and saddle points. J Chem Phys 2000;113:9978–85.
[40] Heyden A, Bell AT, Keil FJ. Efficient methods for finding transition states in chemical reactions: comparison of improved dimer method and partitioned rational function optimization method. J Chem Phys 2005;123:224101.
[41] Riplinger C, Carter EA. Cooperative effects in water binding to cuprous oxide surfaces. J Phys Chem C 2015;119:9311–23.
[42] Bendavid LI, Carter EA. CO_2 adsorption on $Cu_2O(111)$: A DFT + U and DFT-D Study. J Phys Chem C 2013;117:26048–59.
[43] Gao Z, Yang W, Ding X, Ding Y, Yan W. Theoretical research on heterogeneous reduction of N_2O by char. Appl Therm Eng 2017;126:28–36.
[44] Gao S, Sun Z, Liu W, Jiao X, Zu X, Hu Q, et al. Atomic layer confined vacancies for atomic-level insights into carbon dioxide electroreduction. Nat Commun 2017;8:14503.
[45] < https://kinetics.nist.gov/ > .
[46] Manadé M, Viñes F, Illas F. Transition metal adatoms on graphene: a systematic density functional study. Carbon 2015;95:525–34.
[47] Janthon P, Kozlov SM, Vines F, Limtrakul J, Illas F. Establishing the accuracy of broadly used density functionals in describing bulk properties of transition metals. J Chem Theory Comput 2013;9:1631–40.
[48] Krasheninnikov AV, Lehtinen PO, Foster AS, Pyykko P, Nieminen RM. Embedding transition-metal atoms in graphene: structure, bonding, and magnetism. Phys Rev Lett 2009;102:126807.
[49] Yang W, Gao Z, Ding X, Lv G, Yan W. The adsorption characteristics of mercury species on single atom iron catalysts with different graphene-based substrates. Appl Surf Sci 2018;455:940–51.
[50] Wang L, Luo Q, Zhang W, Yang J. Transition metal atom embedded graphene for capturing CO: a first-principles study. Int J Hydrogen Energy 2014;39:20190–6.
[51] Yuan J, Zhang W, Li X, Yang J. A high performance catalyst for methane conversion to methanol: graphene supported single atom Co. Chem. Commun. 2018;54:2284–7.
[52] < https://en.wikipedia.org/wiki/ > .
[53] Zhang H, Liu J, Shen J, Jiang X. Thermodynamic and kinetic evaluation of the reaction between NO (nitric oxide) and char(N) (char bound nitrogen) in coal combustion. Energy 2015;82:312–21.
[54] Zhou Z, Zhang X, Zhou J, Liu J, Cen K. A molecular modeling study of N_2 desorption from NO heterogeneous reduction on Char. Energy Sources, Part A 2013;36:158–66.